Texture-Aware Deblurring for Remote Sensing Images Using ℓ_0-Based Deblurring and ℓ_2-Based Fusion

Heunseung Lim, *Student Member, IEEE*, Soohwan Yu, *Student Member, IEEE*, Kwanwoo Park, Doochun Seo, and Joonki Paik, *Senior Member, IEEE*

***Abstract*—This article presents an image deblurring method using ℓ_0-norm-based deblurring and ℓ_2-norm-based texture-aware image fusion for remote sensing images. To restore the details of blurred texture, the proposed method first performs texture restoration by fusing the restored results using Richardson–Lucy deconvolution and unsharp masking. Next, we analyzed the intensity and dark channel properties of remote sensing images and perform the ℓ_0-norm-based deblurring using the intensity and dark channel priors. Although the ℓ_0-norm-based deblurring can provide a significantly restored result, it cannot overcome the loss of the texture region. On the other hand, the proposed ℓ_2-norm-based image fusion method can preserve both sharp edges and texture details. In the experiments, we demonstrate that the proposed method can provide better restored results than existing state-of-the-art deblurring methods without oversmoothing and undesired artifact.**

***Index Terms*—Deblur, remote sensing, image restoration.**

I. Introduction

VERY high-resolution remote sensing images are widely used in many fields such as earth observation, land monitoring, and topography observation [1]–[11]. However, the acquired raw image is severely degraded by various factors including atmospheric turbulence, cloud, and defocusing, to name a few [12]. The point spread function (PSF) also takes into consideration other degradation factors such as atmospheric turbulence, defocusing, and blurring. In addition, we further considered aliasing artifacts due to frequency folding when subsampling during the image acquisition process. Since the image degradation artifact generates geometric distortion, an accurate location of important objects depends on computer vision algorithms such as object detection. To solve this problem, many types of research have been proposed to estimate PSF and restore the blurred image. The image restoration problem is formulated as follows.

Given an $N \times N$ latent image that is an ideal, undegraded version, the observed image is obtained by convolving the latent image with a PSF of the imaging system and additive noise. The matrix-vector representation of the image degradation model is given as

$$g = SHf + \eta \tag{1}$$

where g, f, and η are $N^2 \times 1$ vectors representing the observed, latent, and additive Gaussian noise images, respectively, and H the $N^2 \times N^2$ block-circulant matrix generated from a PSF. S is an $N \times N$block diagonal matrix that performs the subsampling operation. When the PSF and noise variance are given, the problem in (1) is a simple deconvolution whereas it becomes a blind deconvolution problem if the PSF and noise variance are unknown. H represents PSF that depends on the remote sensing system in (1). More specifically, the PSF of remote sensing images is a linear combination of Gaussian functions [13], [14]. For that reason, our PSF is assumed to be a single Gaussian function, and as a result, the corresponding objective assessments used a Gaussian low-pass filter.

In the blind deconvolution problem of the remote sensing, a straightforward way to estimate the PSF is to use a specified edge target acquired by artificial installation on the ground. Another approach is to locate a sharp edge, which is considered as a blurred version of the ideal step edge, in the observed image. Shen *et al.* proposed an edge detection method to locate and estimate the PSF [15]. More specifically, they detected knife-edges using the alternating minimization framework and then estimated parameters of the PSF. Azadbakht *et al.* proposed sparsity-constrained regularization method and used L-curve to determine the optimal regularization parameters for efficient target extraction [16].

Since blind deconvolution is an ill-posed problem, various regularization approaches have been proposed in the literature including Wiener filter and Richardson–Lucy algorithm [17], [18]. Although these methods provide the restored results at low computational cost, it cannot overcome the inherent restoration artifact such as amplified ringing around strong edges when the PSF is inaccurately estimated. Shan *et al.* used a camera model parameters to eliminate camera induced degradation [19], and Fergus *et al.* estimated PSF using the Bayesian

Manuscript received March 30, 2020; revised May 26, 2020; accepted June 1, 2020. Date of publication June 4, 2020; date of current version June 22, 2020. This work was supported by the Korea Aerospace Research Institute (NRF-2017M1A3A4A07028434). *(Heunseung Lim and Soohwan Yu contributed equally to this work.) (Corresponding author: Joon Ki Paik.)*

Heunseung Lim, Soohwan Yu, and Joonki Paik are with the Department of Image, Chung-Ang University, Seoul 06974, South Korea (e-mail: hslim0214@cau.ac.kr; shyu@cau.ac.kr; paikj@cau.ac.kr).

Kwanwoo Park is with the Autonomous Driving Lab, PLK Technology, 314, Seongnam-si 13591, South Korea (e-mail: rhdn4375@plk.co.kr).

Doochun Seo is with the Department of Satellite Data Cal/Val Team, Korea Aerospace Research Institute, Daejeon 34133, South Korea (e-mail: dcivil@kari.re.kr).

Digital Object Identifier 10.1109/JSTARS.2020.2999961

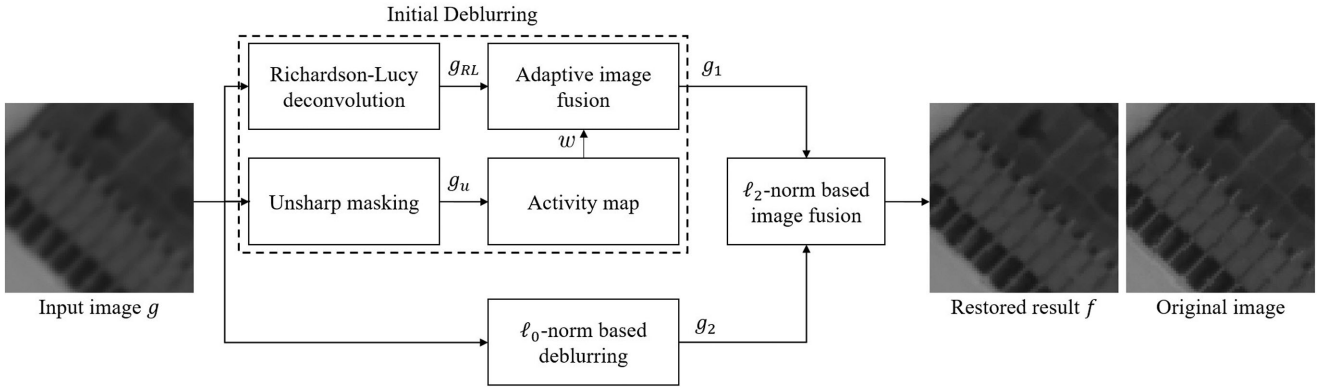

Fig. 1. Block diagram of the proposed deblurring algorithm.

formula [20]. Yuan *et al.* solved the blind deconvolution problem using the edge sharpness information with Tikhonov regularization [21].

Another approach is to use the constraint in the optimization problem. Xu *et al.* minimized ℓ_0-norm using the half-quadratic splitting method and effectively restored a blurred image [22]. Krishnan *et al.* presented the ℓ_1 and ℓ_2 constraint terms to impose the scale-invariant sparsity to the high-frequency band in the blur kernel estimation step. More specifically, they estimated the blur kernel estimation by minimizing an energy functional including ℓ_1 and ℓ_2 constraint terms using iterative shrinkage-thresholding algorithm [23]. An alternative approach is to use the Huber–Markov prior model, which combines the advantages of the total variation and Tikhonov regularization [24]. Perrone *et al.* proposed total variation-based PSF estimation in the iterative manner and restored a blurred image using the projected alternating minimization algorithm [25]. Zhu *et al.* used multiple frames to improve the quality of a video, which was acquired by a ground-based telescope. They aligned a set of frames using nonrigid registration and performed near-diffraction-limited restoration and blind deconvolution [12].

Various deblurring methods have been developed and provided well-restored remote sensing images to some extent. However, the restored remote sensing images lose important texture information and have undesired ringing artifact near edges. To solve this problem, this article presents an image fusion-based restoration method for the remote sensing images. The proposed method consists of three steps: 1) initial deblurring using adaptive image fusion, 2) ℓ_0-norm-based deblurring, and 3) ℓ_2-norm-based image fusion. Since the proposed method combines the results of the initially deblurred image and its refined version based on the ℓ_0-norm, the resulting image can preserve both texture and edge regions. Experimental results show that the proposed method well-preserved texture regions without ringing artifacts. Fig. 1 shows the block diagram of the proposed deblurring method.

The rest of this article is organized as follows. Section II describes the proposed deblurring method including three functional modules. Experimental results are shown in Section III, and Section IV concludes this article.

II. Proposed Method

A. Texture Restoration Using Adaptive Fusion

To generate a texture-restored image, the proposed method adaptively combines the results of Richardson–Lucy and unsharp masking methods [18], [26]. The Richardson–Lucy algorithm iteratively restores the blurred input image based on Bayes' theorem, but it cannot solve the tradeoff problem between noise amplification and ringing artifacts near edges. To solve this problem, the proposed method adds the result of unsharp masking in the manner of adaptive image fusion [27], where the activity map represents the ratio which is inversely proportional to the local variance as

$$w(\mathbf{x}) = \frac{1}{1 + \kappa v(\mathbf{x})} \tag{2}$$

where $\mathbf{x} = [x, y]^T$ represent the pixel coordinates, $w(\mathbf{x})$ is the activity map, $v(\mathbf{x})$ the local variance, and κ the tuning parameter to make $w(\mathbf{x})$ distributed as evenly as possible.

As shown in Figs. 2 and 3, the effect of unsharp masking is reduced by adaptive fusion. However, if there is zero-intensity in the original image, the unsharp masking result will have negative intensity, which results in undesired artifacts such as dark halo near edges. For that reason, a 2-D derivative filter for unsharp masking was empirically selected using MATLAB "fspecial function" with "unsharp" and $\alpha = 0.1$.

Fig. 2 shows the estimated activity map using the result of unsharp masking. Since the activity value is low in the edge region with high local variance, the activity map can efficiently attenuate the ringing artifact caused by Richardson–Lucy restoration while preserving the edge region of unsharp masking. In addition, it can also preserve the texture region of the result of Richardson–Lucy algorithm. The result of texture restoration, denoted as g_1 is obtained using the estimated activity map as

$$g_1(\mathbf{x}) = (1 - w(\mathbf{x}))g_{RL}(\mathbf{x}) + w(\mathbf{x})g_u(\mathbf{x}) \tag{3}$$

where g_{RL} and g_u, respectively, represent the result of Richardson–Lucy deconvolution and unsharp masking. Fig. 3 shows the step-by-step results of texture restoration. As shown in Fig. 3(c), the result of Richardson–Lucy deconvolution exhibits

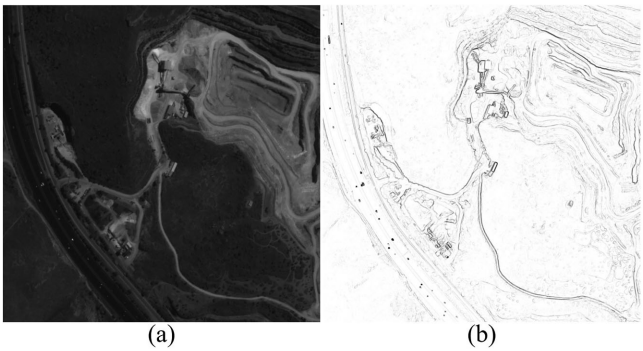

Fig. 2. Estimated activity map using the result of unsharp masking: (a) unsharp masking and (b) activity map.

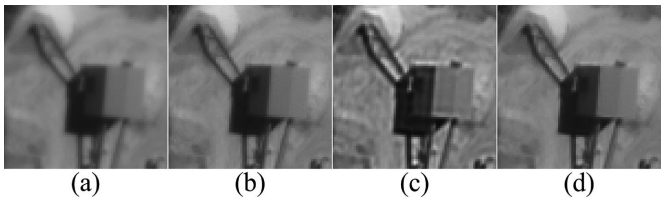

Fig. 3. Step by step results of texture restoration: (a) an input image, (b) result of unsharp masking, (c) result of Richardson–Lucy deconvolution, and (d) result of texture restoration.

undesired ringing artifact and noise amplification, whereas it can better preserve the texture region than that of unsharp masking as shown in Fig. 3(b). On the other hand, Fig. 3(d) shows the better restored result without undesired ringing artifacts in the edge region while preserving texture details using the adaptive image fusion with the activity map. In addition, it can suppress noise amplification using the adaptive image fusion with the result of unsharp masking.

B. ℓ_0-Norm-Based Deblurring Using Intensity and Dark Channel Priors

In this section, we present a novel deblurring method that combines the intensity and dark channel priors (DCP). The DCP is based on a statistical assumption that at least one intensity value among R, G, and B pixels is close to zero in the natural scene [28]. Pan *et al.* demonstrated that a sharp image shows more dark channel pixels than a blurred image, which means that the dark channel pixels on the latent sharp image show more sparsity than a blurred image. They performed an image deblurring using the DCP as a prior knowledge to a latent sharp image [29]. Fig. 4 shows the comparison of the dark channel maps of sharp and blurred images. As shown in the figure, the sharp image has more dark channel pixels than the blurred one.

Pan *et al.* proposed a text image deblurring algorithm using the intensity prior, which assumes that the histogram of a sharp image has a larger number of bins at the highest intensity level than that of a blurred image [30]. We analyzed the intensity distribution property of 230 PAN-band remote-sensing images, which were acquired by Korea Multi-Purpose Satellite-3A (KOMPSAT-3A) earth observation satellite. The blurred version was generated using a Gaussian low-pass filter of size 65×65 with a standard deviation $\sigma = 7$. Fig. 4(c) and (f) shows the intensity histogram of Fig. 4(a) and (d).

As shown in the figure, the intensity histogram of the sharp image has a larger number of bins at the lower intensity levels than the blurred image. In [29], Pan *et al.* demonstrated that a clean image has fewer bright intensity pixels than its blurred version. This property can be expressed as

$$B(\mathbf{x}) = \sum_{z \in \Omega_H} H(\mathbf{z}) f\left(\mathbf{x} + \left[\frac{s}{2}\right] - \mathbf{z}\right) \geq H(\mathbf{z}') f\left(\mathbf{x} + \left[\frac{s}{2}\right] - \mathbf{z}'\right) > 0 \tag{4}$$

where $H(\mathbf{z}) \geq 0$, $\sum H(\mathbf{z}) = 1$, Ω_H is the domain of the blur kernel, s the size of blur kernel, and $[\cdot]$ the rounding operator. It means that zero intensity pixels are removed by the convolution with blur kernel for a pixel $\mathbf{z}' \in \Omega_H$, which satisfies the condition of $H(\mathbf{z}') \neq 0$ and $f(\mathbf{x} + [\frac{s}{2}] - \mathbf{z}') \neq 0$ [29]. This property does not consider the trivial case that the sharp image only has zero intensity pixels in the large area. For that reason, it also satisfies $\|g\|_0 > \|f\|_0$.

We incorporate both intensity and dark channel priors in the form of regularization terms, which enforce the sparsity of the latent image. The proposed energy functional is expressed as

$$\min_f \|Hf - g\|_2^2 + \alpha \|\nabla f\|_0 + \beta \|f\|_0 + \lambda \|D(f)\|_0 \tag{5}$$

where ∇ is the $N^2 \times N^2$ block-circulant matrix representing the 2-D derivative operator, $D(\cdot)$ an operator to estimate the dark channel map, and α, β, and λ are penalty parameters for the gradient, intensity prior, and dark channel prior, respectively.

In (5), the regularization terms $\|f\|_0$ and $\|D(f)\|_0$ commonly make pixel intensity values converge to zero. This property is based on the property that a blurred image tends to include more bright intensity than its sharper version, and vice versa. This property is inferred from dark channel prior, which has been proved in the field of image dehazing research. Although remote sensing images have more complex histograms than a consumer photography or text image, histograms of blurred remote sensing images also have a higher intensity than sharp images. In this context, minimization of $\|f\|_0$ in (5) helps make the solution image look sharper. Along the same lines, dark channel prior assures that a sharp image has more dark pixels than blurred images, and minimization of ℓ_0-norm of the dark channel map, that is, $\|D(f)\|_0$ in (5), makes the solution image have more dark pixels. The proposed method incorporates the dark channel and intensity priors in the form of ℓ_0-regularization terms to deblur remote sensing images.

The proposed energy functional is nonconvex and nondifferentiable due to a ℓ_0-regularization terms and nonlinearity of $D(\cdot)$. To minimize the proposed objective function, we employ the half-quadratic splitting ℓ_0-minimization method [31]. Since

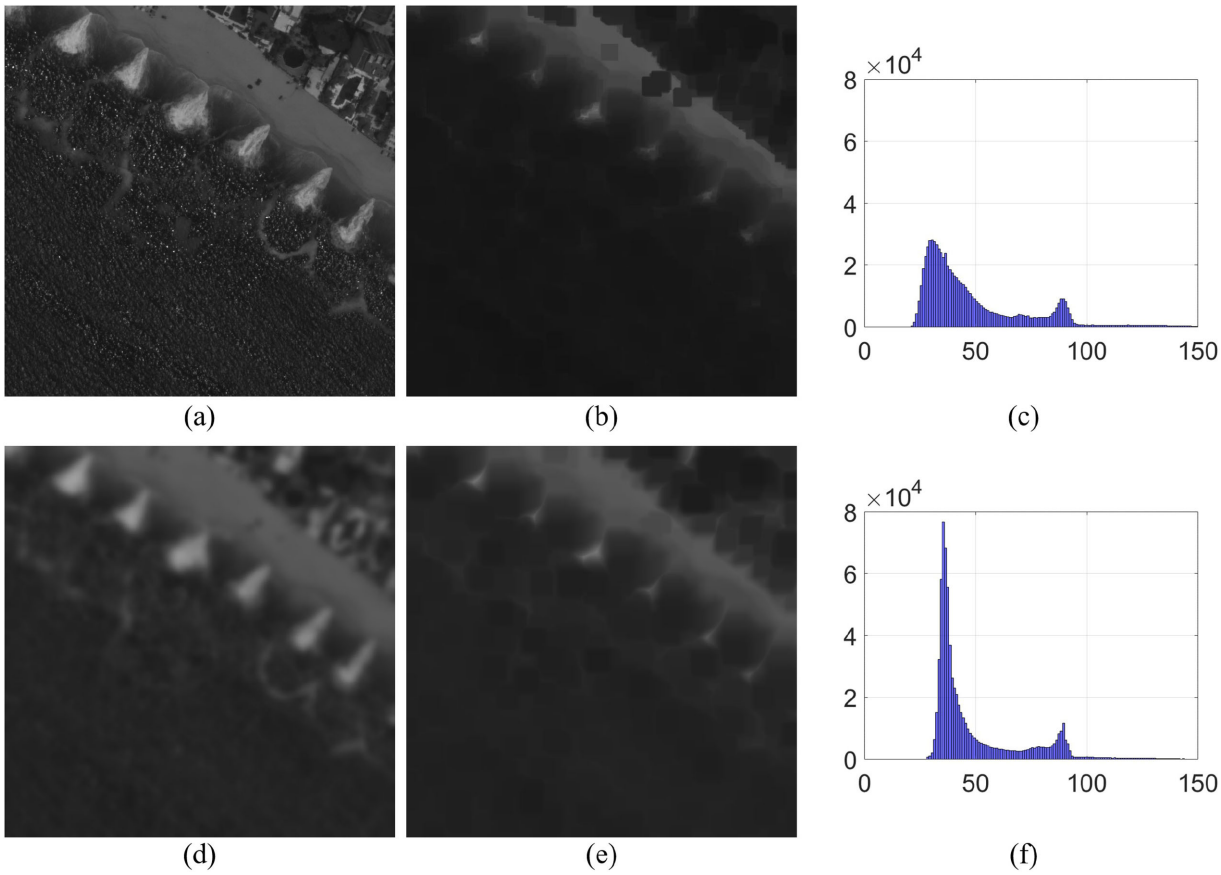

Fig. 4. Illustration of blurring effect to dark channel and histograms: (a) a sharp image, (b) dark channel of (a), (c) intensity histogram of (a), (d) a blurred image, (e) dark channel of (d), and (e) intensity histogram of (d).

(5) has three ℓ_0 terms, its splitting version needs the corresponding auxiliary variables as

$$\min_{f,d,u,p} \|Hf - g\|_2^2 + \alpha\|\nabla f - d\|_2^2 + \beta\|f - u\|_2^2 + \lambda\|D(f) - p\|_2^2 + \mu\|d\|_0 + \omega\|u\|_0 + \gamma\|p\|_0 \quad (6)$$

where μ, ω, and γ are the regularization parameters. Equation (6) can be solved using alternative minimization of splitted subproblems with respect to f, d, u, and p.

1) f-Related Subproblem: The subproblem related to f with d, u, and p fixed is simplified as

$$\min_f \|Hf - g\|_2^2 + \alpha\|\nabla f - d\|_2^2 + \beta\|f - u\|_2^2 + \lambda\|D(f) - p\|_2^2 \quad (7)$$

where

$$D(f) = \min_{y\in\Omega(\mathbf{x})} \left(\min_{c\in(r,g,b)} f^c(y) \right) \quad (8)$$

where $\Omega(\mathbf{x})$ is an image patch centered at $\mathbf{x}$.

Although the subproblem in (7) is a quadratic function, its optimality condition cannot be represented as a linear equation because $D(\cdot)$ is a nonlinear function. To solve this problem, Pan *et al.* approximated the nonlinear function using a linear operator $\mathbf{M}$ as [29]

$$\mathbf{M}(\mathbf{x},\mathbf{z}) = \begin{cases} 1, & \mathbf{z} = \arg\min_{\mathbf{z}\in\Omega(\mathbf{x})} f(\mathbf{z}) \\ 0, & \text{otherwise} \end{cases} \quad (9)$$

which is computed by comparing the location of dark channel pixels of the previous intermediate latent image at each iteration. Fast minimization of (7) is possible using the diagonalization property of the fast Fourier transform (FFT) [29], [32], [33].

2) d, p, u-Related Subproblem: The subproblems related to d, p, and u with f fixed are respectively defined as

$$\min_d \alpha\|\nabla f - d\|_2^2 + \mu\|d\|_0 \quad (10)$$

$$\min_p \lambda\|D(f) - p\|_2^2 + \gamma\|p\|_0 \quad (11)$$

and

$$\min_u \beta\|f - u\|_2^2 + \omega\|u\|_0. \quad (12)$$

According to [31], the subproblems (10)–(12) have become their own closed-form solution that can be computed using elementwise minimization as

$$d = \begin{cases} \nabla f, & |\nabla f|^2 \le \mu/\alpha \\ 0, & \text{otherwise} \end{cases} \quad (13)$$

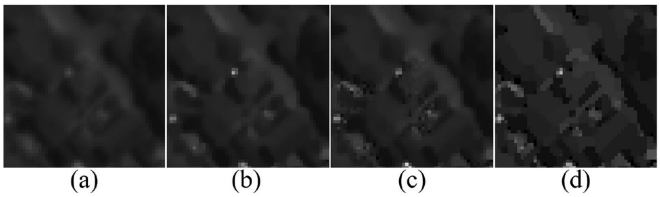

Fig. 5. Comparison of resulting images: (a) an input image, (b) Pan's method [29], (c) Pan's method [30], and (d) the proposed method.

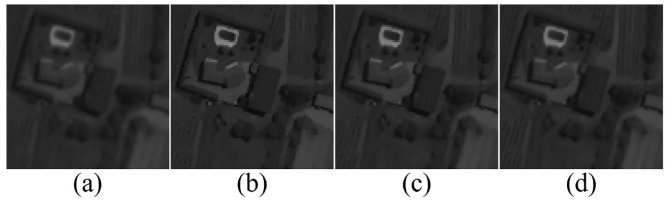

Fig. 6. Comparative results using different values of parameter τ: (a) an input image, (b) $\tau = 1$ (c) $\tau = 3$, and (d) $\tau = 10$.

$$p = \begin{cases} D(f), & |D(f)|^2 \leq \gamma/\lambda \\ 0, & \text{otherwise} \end{cases} \tag{14}$$

and

$$u = \begin{cases} f, & |f|^2 \leq \omega/\beta \\ 0, & \text{otherwise .} \end{cases} \tag{15}$$

Fig. 5 shows the comparison of the restored results using existing state-of-the-art and proposed methods based on ℓ_0-norm minimization. More specifically, Fig. 5(b) shows the result of Pan's method using only dark channel prior [29], where we can observe blurring artifacts near edges. Fig. 5(c) shows the result of Pan's deblurring method using only intensity prior [30], which results in undesired artifact near edges. On the other hand, the proposed method can provide better-restored result with sharp edges than existing methods as shown in Fig. 5(d).

C. Image Fusion by Minimizing ℓ_2 Loss

Although the ℓ_0-norm-based deblurring can significantly improve the restoration performance while preserving the strong edges, it loses texture details by oversmoothing. To preserve both strong edge and texture details, we adaptively fuse the texture restored and ℓ_0-norm-based deblurred results. Specifically, we minimize the following ℓ_2-norm-based loss function

$$\min_f \|f - g_2\|_2^2 + \tau \|f - g_1\|_2^2 \tag{16}$$

where f is the latent image to be restored, g_2 the resulting image of ℓ_0-norm-based deblurring, and g_1 the result of texture restoration. τ represents a nonnegative parameter to control the balance between the results g_1 and g_2. Minimizing the first term in (16) makes the restored result f preserve the strong edges, while minimizing the second term makes the restored result consistent with the texture restored result. Since (16) is a quadratic minimization problem, we can obtain the solution using FFT as

$$f = \mathcal{F}^{-1}\left(\frac{\mathcal{F}(g_2) + \tau \mathcal{F}(g_1)}{1 + \tau}\right) \tag{17}$$

where $\mathcal{F}$ and $\mathcal{F}^{-1}$ represent the FFT and inverse FFT operations, respectively.

In addition, Fig. 6 shows the restored results with different values of τ. As shown in the figure, a small τ tends to preserve strong edges at the cost of losing texture details, and vice versa. Based on visual observation, $\tau \in [0, 4.0]$ is the experimentally best choice.

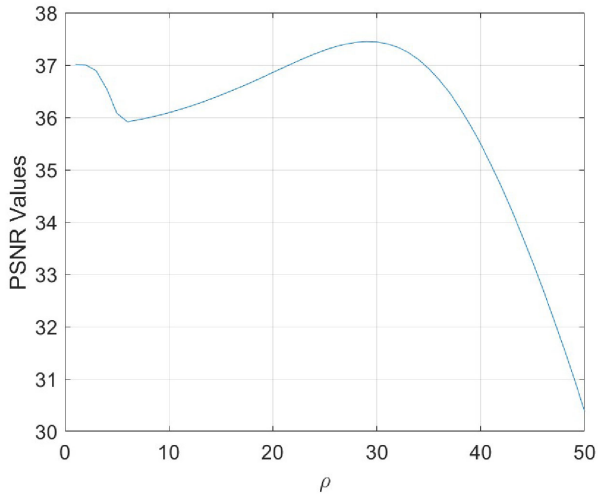

Fig. 7. Deblurring results in PSNR values using estimated Gaussian PSF versus parameter ρ.

D. PSF Estimation

In this article, we used an ℓ_1-norm minimization method to estimate the PSF, and the energy functional is defined as

$$\min_H \|Hf - g\|_2^2 + \rho \|H\|_1, \text{subject to } H_i \geq 0, \sum_i H_i = 1 \tag{18}$$

where ρ is a nonnegative regularization parameter. The energy functional of (18) is convex, but it is not differentiable because of the ℓ_1-norm. To solve this problem, we used an interior-point method proposed by Kim *et al.* [34]. More specifically, we used Figs. 8(a)–(h) to find the suitable ρ and to estimate the best Gaussian low-pass filter that approximates the reference PSF. As a result, the range of ρ is $[1.0, 50.0]$, Gaussian low-pass filter is of size 7×7 with a standard deviation $\sigma = 1$. Fig. 7 shows the estimated PSNR values of PSF for ρ values, with the highest value at $\rho = 29$. Based on these experiments, we set the ρ value.

III. Experimental Results

This section demonstrates the image deblurring performance of the proposed method by comparing with existing state-of-the-art methods including Krishnan's method [23], Perrone's method [25], Pan's method in 2016 [29], and another Pan's method in 2017 [30]. The experiments were performed using a personal computer with a CPU speed of 3.70 GHz and a

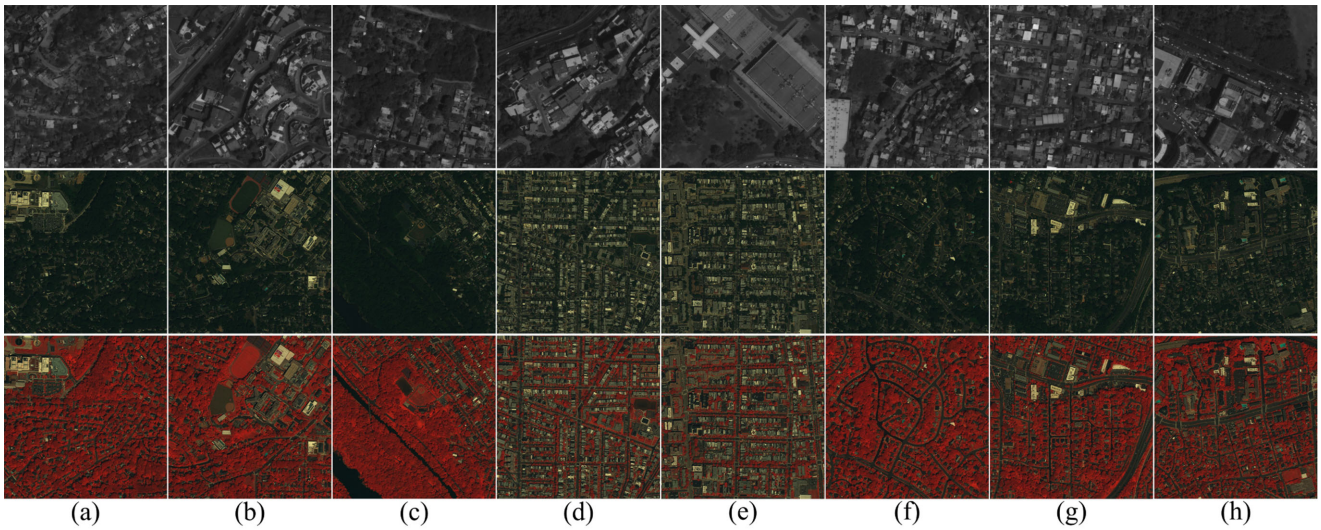

Fig. 8. Set of PAN, RGB, and NGB band images acquired by WorldView-2 and WorldView-4 earth observation satellite. (a)–(h) were used in the objective assessments of the proposed method and summarized in Table I.

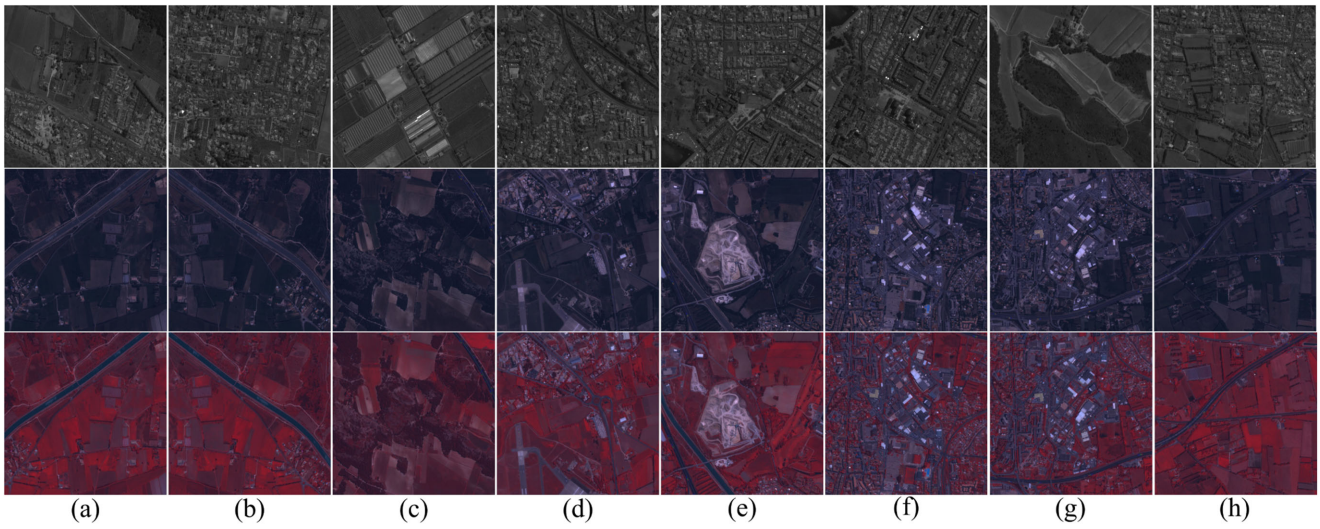

Fig. 9. Set of PAN, RGB, and NGB band images acquired by KOMPSAT-3A earth observation satellite. (a)–(h) were used in the objective assessments of the proposed method and summarized in Table II.

64GByte RAM. In addition, we empirically set the regularization parameters to compute (13)–(15) to $\alpha = 10^5$, $\beta = 8$, and $\lambda = 8$, respectively. The proposed PSF estimation method uses the method described in Section II-D. On the other hand, other PSF estimation methods use their own method. In experiments for deblurring of multispectral band, we assumed that the input multispectral band images were blurred by the same PSF.

A. Simulated Data

We performed the objective assessment using peak signal-to-noise ratio (PSNR) and structural similarity index measure (SSIM) [35]. We used a set of test remote sensing images acquired by WorldView-2 and WorldView-4 earth observation satellite [36]. Specifically, we used panchromatic (PAN) band images of size $16\,384 \times 16\,384$, and cropped them to 850×850 as shown in Fig. 8. In addition, red, green, blue, and near-infrared band images of size 2048×2048 were cropped down to 450×450 as shown in Fig. 8. The second and third rows of Fig. 8 respectively show red, green, and blue (RGB), and near-infrared, green, and blue (NGB) band images. To evaluate the objective performance of deblurring, we synthetically generated blurred images using a Gaussian low-pass filter of size 7×7 with a standard deviation $\sigma = 1$. The downsampled, deblurred results are resampled to the resolution of the original image. Figs. 10 and 11 show the comparative deblurring results on the blurred images, which were synthesized using Fig. 8(d), (e), and (f). Krishnan's and Perrone's methods provided the deblurring results that preserve the texture details but cannot restore the strong edge regions as shown in Figs. 10(c)–11(c).

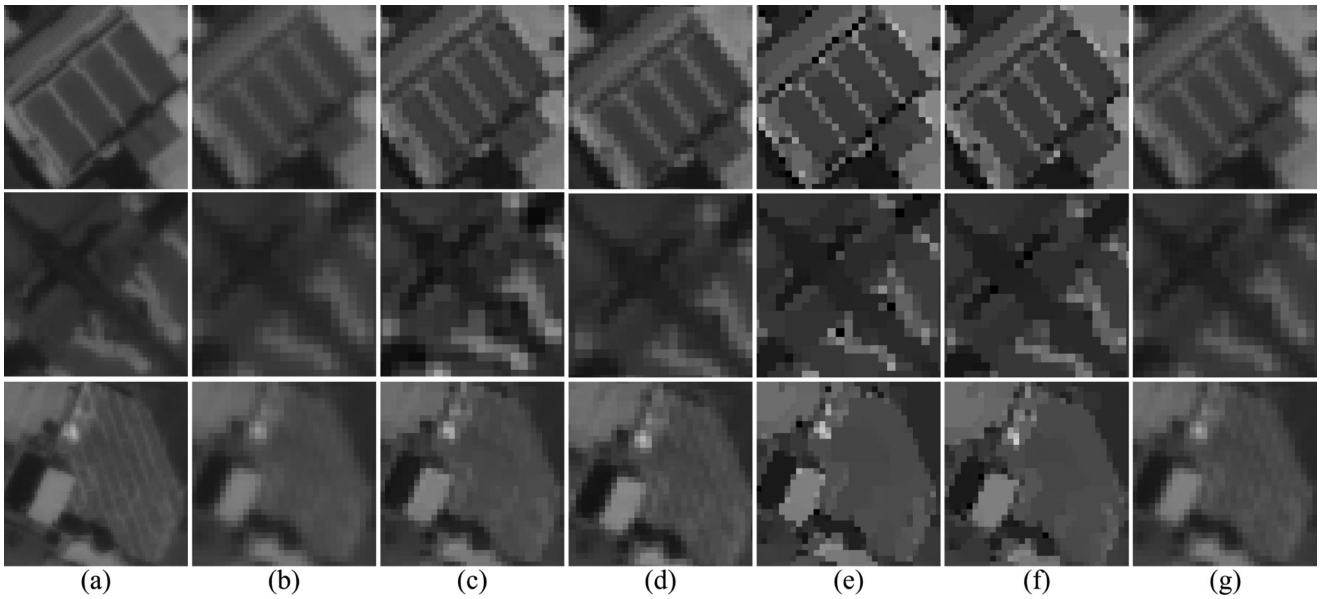

Fig. 10. Comparative results on the synthesized blurred image using PAN band: (a) an original image, (b) a blurred image by Gaussian low-pass filter, (c) Krishnan's method [23], (d) Perrone's method [25], (e) Pan's method [29], (f) Pan's method [30], and (g) the proposed method ($\mu = 10^{-5}$, $\omega = 10^{-6}$, $\gamma = 9.61 \times 10^{-4}$, and $\tau = 3.1$). The results are better viewed in zoomed mode.

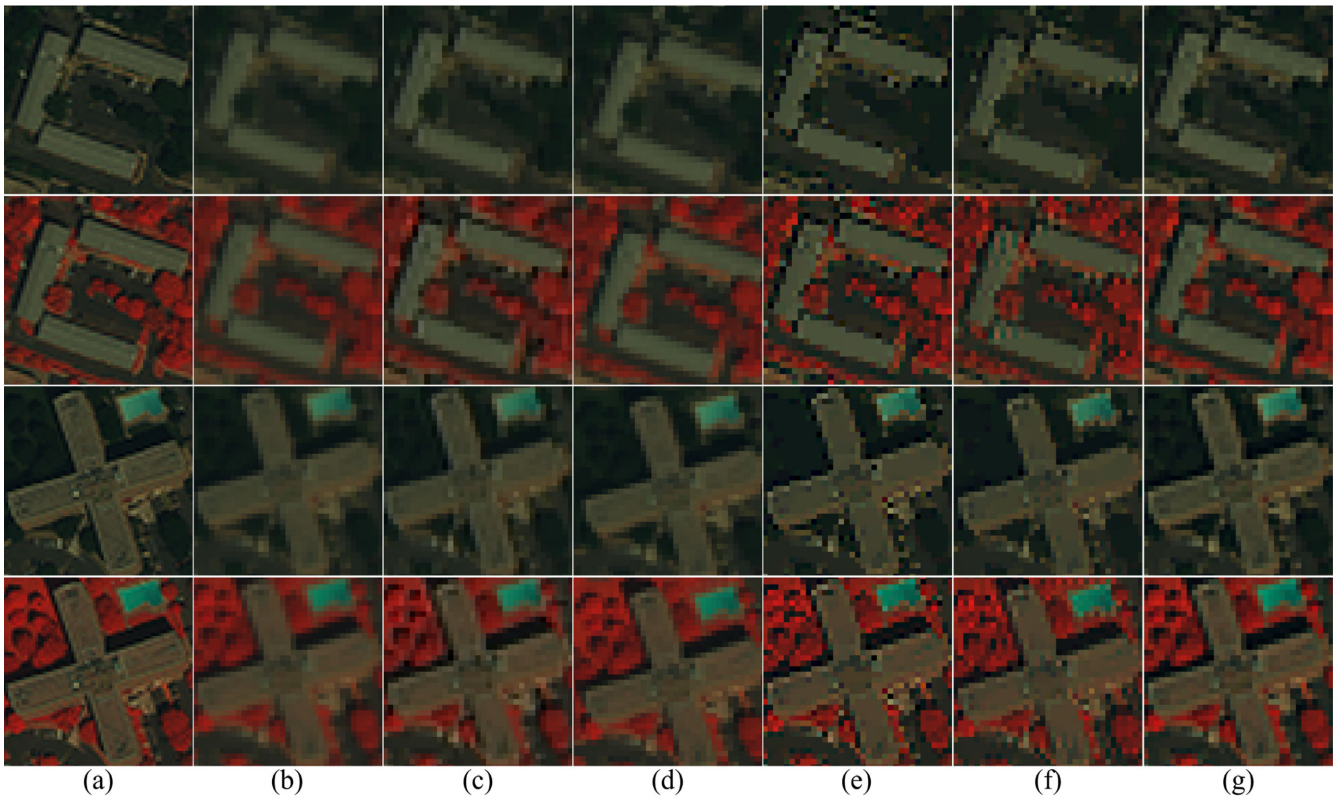

Fig. 11. Comparative results on the synthesized blurred image using RGB and NGB bands: (a) an original image, (b) a blurred image by Gaussian low-pass filter, (c) Krishnan's method [23], (d) Perrone's method [25], (e) Pan's method [29], (f) Pan's method [30], and (g) the proposed method ($\mu = 10^{-5}$, $\omega = 10^{-6}$, $\gamma = 10^{-6}$, and $\tau = 2.1$). The results are better viewed in zoomed mode.

TABLE I
OBJECTIVE EVALUATION OF THE DEBLURRING PERFORMANCE USING PSNR AND SSIM [35]

		[23]		[25]		[29]		[30]		Proposed	
		PSNR	SSIM	PSNR	SSIM	PSNR	SSIM	PSNR	SSIM	PSNR	SSIM
Fig. 8(a)	PAN	32.25	0.8777	28.39	0.7818	31.42	0.8524	30.24	0.8239	**36.53**	**0.9357**
	RGB	25.56	0.7305	22.34	0.6462	**26.11**	**0.7859**	23.92	0.7065	25.38	0.7855
	NGB	**21.83**	0.6964	15.44	0.5437	18.03	0.7199	16.66	0.6006	18.56	**0.7322**
Fig. 8(b)	PAN	33.13	0.9203	23.85	0.7145	27.00	0.8251	27.11	0.7968	**33.89**	**0.9271**
	RGB	**27.25**	**0.7971**	22.05	0.6155	24.30	0.7419	22.45	0.6504	24.17	0.7544
	NGB	**20.05**	0.5737	15.75	0.5251	17.47	0.6838	16.90	0.5677	18.71	**0.7125**
Fig. 8(c)	PAN	31.56	0.8760	28.56	0.7822	30.76	0.8501	34.66	0.9275	**36.46**	**0.9384**
	RGB	**30.08**	0.8572	25.24	0.7564	27.21	0.8213	25.89	0.7781	27.29	0.8363
	NGB	**21.03**	0.6456	16.69	0.6214	19.32	0.7453	17.31	0.6464	19.10	**0.7608**
Fig. 8(d)	PAN	29.87	0.8676	23.01	0.6894	26.42	0.8136	27.16	0.8052	**34.25**	**0.9326**
	RGB	21.91	0.5281	18.28	0.3803	22.42	0.6730	19.71	0.4842	**23.37**	**0.7268**
	NGB	20.19	0.5285	16.32	0.3673	19.57	0.6581	17.03	0.4519	**21.04**	**0.7160**
Fig. 8(e)	PAN	31.21	0.8830	29.63	0.8486	31.55	0.8913	29.45	0.8445	**36.84**	**0.9459**
	RGB	**24.35**	0.6835	18.54	0.3883	22.62	0.6797	19.89	0.4935	23.49	**0.7286**
	NGB	**22.35**	0.6795	16.76	0.3754	20.05	0.6647	17.88	0.4727	21.43	**0.7169**
Fig. 8(f)	PAN	29.88	0.8523	25.93	0.7308	28.45	0.8294	26.80	0.7738	**34.00**	**0.9227**
	RGB	27.56	0.7456	24.51	0.6675	27.46	0.7885	25.59	0.7136	**28.49**	**0.8344**
	NGB	**20.71**	0.6571	15.83	0.5673	17.83	0.7228	16.49	0.6121	20.32	**0.7894**
Fig. 8(g)	PAN	30.08	0.8529	24.33	0.6767	26.99	0.7940	27.01	0.7706	**33.74**	**0.9197**
	RGB	25.25	0.6740	21.61	0.5748	24.98	0.7294	23.36	0.6437	**26.34**	**0.7887**
	NGB	20.13	0.5748	15.54	0.5010	18.44	0.6917	16.36	0.5630	**20.29**	**0.7584**
Fig. 8(h)	PAN	33.49	0.9272	25.23	0.7401	27.63	0.8365	27.46	0.8216	**34.26**	**0.9313**
	RGB	25.10	0.6466	21.97	0.5542	25.01	0.7250	23.25	0.6212	**26.17**	**0.7785**
	NGB	**22.19**	0.6917	15.88	0.4886	18.86	0.6926	17.12	0.5628	20.55	**0.7541**
Avg.	PAN	31.43	0.8821	26.12	0.7455	28.78	0.8365	28.74	0.8205	**35.00**	**0.9317**
	RGB	**25.88**	0.7078	21.82	0.5729	25.01	0.7431	23.01	0.6364	25.59	**0.7791**
	NGB	**21.06**	0.6309	16.02	0.4987	18.70	0.6974	16.97	0.5596	20.00	**0.7425**

Although Pan's method using only the dark channel prior shows better deblurred result than Krishnan's and Perrone's methods at the strong edge regions, it cannot preserve the texture details of the diagonal patterns existing in the original image as shown in Figs. 10(a)–11(a). In the same manner, Pan's method based on the intensity prior cannot preserve the texture details as shown in Figs. 10(f)–11(f). On the other hand, the proposed method shows almost the best deblurred results, which is consistent to the texture details of the diagonal pattern in the original image and at the same time preserves the strong edges as shown in Figs. 10(g)–11(g).

Table I shows the objective evaluation using PSNR and SSIM. As summarized in Table I, since the proposed method adaptively fuses the texture details using ℓ_2-norm minimization preserving the restored strong edges, the averaged PSNR and SSIM values are higher than existing deblurring methods [12].

B. Real Data

In this section, we perform the evaluation of the deblurring performance using the PAN band remote sensing images acquired by KOMPSAT-3A. We cropped each PAN band image of size $24\,000 \times 24\,600$ to 850×850 as shown in Fig. 9. The RGB and NGB band images of size 3020×3000 were cropped to 450×450 as shown in the second and third rows of Fig. 9, respectively.

Fig. 12 compare deblurring results using Fig. 9(a), (e), and (g). Krishnan's and Perrone's methods provided better restored texture regions than those of Pan's methods, but they still show weak restoration performance at the strong edges. Although Pan's methods using both intensity and dark channel priors successfully restore the sharp edges, they cannot overcome the oversmoothing problem as shown in Fig. 12(d)– (e)–13(d)–(e). On the other hand, the proposed method shows improved restoration performance in terms of preserving the texture details with the sharp edges than existing deblurring methods as shown in Figs. 12(f)–13(f).

In addition, the deblurring performance was evaluated using Q metric [37], which quantifies the amount of image contents based on the singular value decomposition of local gradients. As summarized in Table II, the proposed method provided higher Q metric value than existing methods, which means that the result

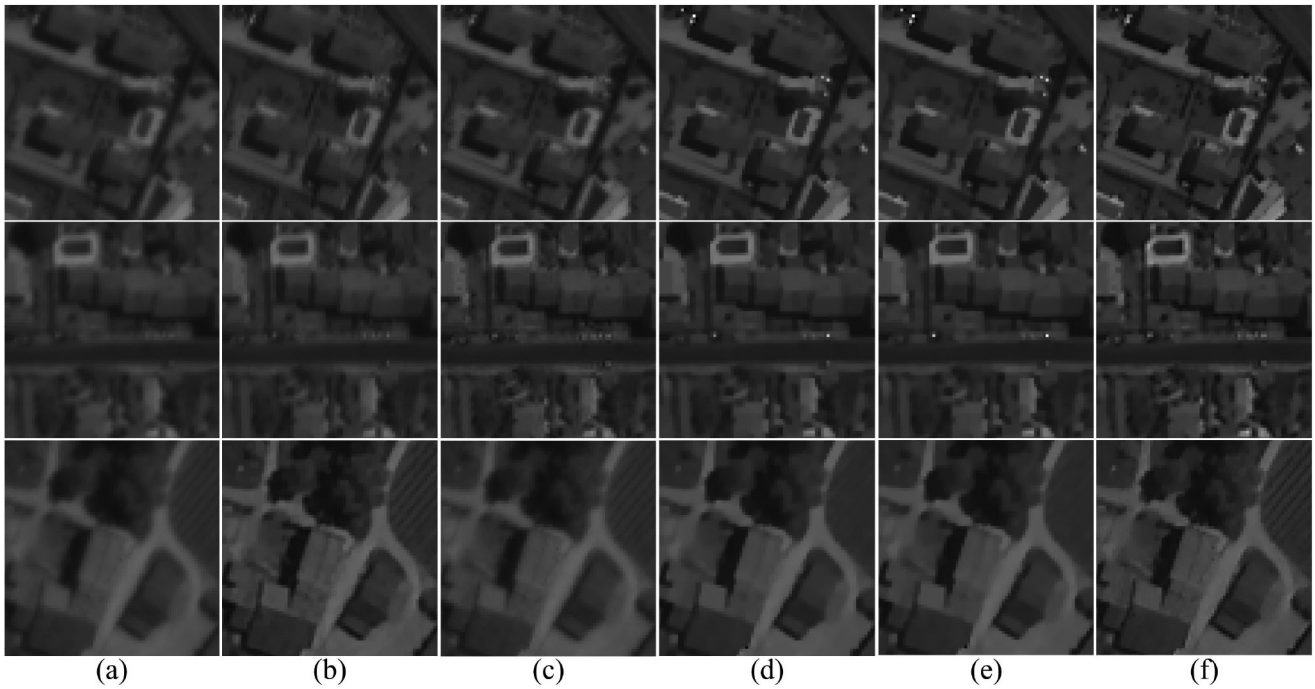

Fig. 12. Comparative results on the real PAN band images: (a) an input image, (b) Krishnan's method [23], (c) Perrone's method [25], (d) Pan's method [29], (e) Pan's method [30], and (f) the proposed method ($\mu = 10^{-5}$, $\omega = 10^{-6}$, $\gamma = 1.61 \times 10^{-4}$, and $\tau = 3.1$). The results are better viewed in zoomed mode.

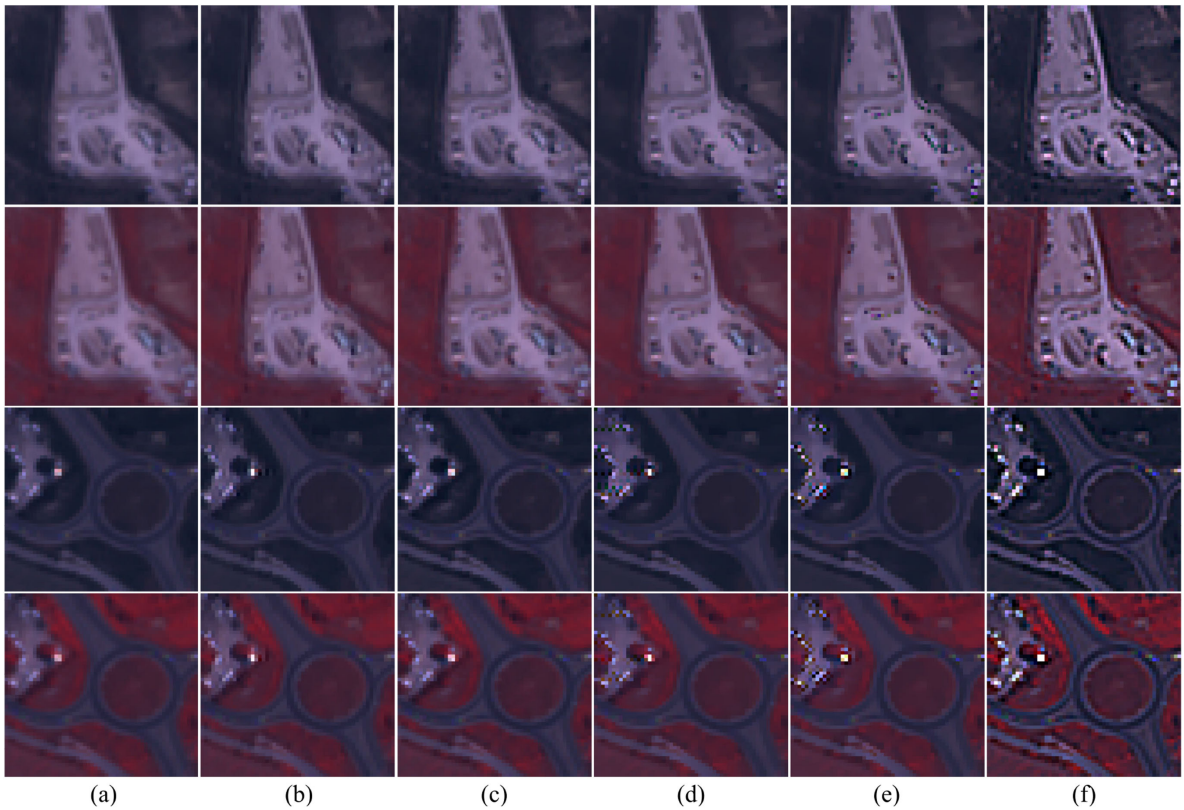

Fig. 13. Comparative results on the real RGB and NGB bands images: (a) an input image, (b) Krishnan's method [23], (c) Perrone's method [25], (d) Pan's method [29], (e) Pan's method [30], and (f) the proposed method ($\mu = 10^{-5}$, $\omega = 10^{-6}$, $\gamma = 1.61 \times 10^{-4}$, and $\tau = 3.5$). The results are better viewed in zoomed mode.

TABLE II
PERFORMANCE EVALUATION USING Q METRIC [37]

		[23]	[25]	[29]	[30]	Proposed
Fig. 9(a)	PAN	11.15	10.58	12.02	12.41	**16.07**
	RGB	11.03	11.34	11.19	13.23	**23.03**
	NGB	10.10	12.07	11.24	13.66	**23.37**
Fig. 9(b)	PAN	11.94	11.49	15.04	15.47	**17.38**
	RGB	11.39	11.69	11.38	13.69	**24.95**
	NGB	10.14	11.90	10.93	14.02	**23.81**
Fig. 9(c)	PAN	13.76	14.32	16.26	**16.60**	16.53
	RGB	9.31	8.55	9.87	10.00	**16.50**
	NGB	8.55	8.37	9.65	9.68	**15.60**
Fig. 9(d)	PAN	12.19	11.77	14.62	14.49	**17.59**
	RGB	11.46	14.11	12.09	14.54	**24.00**
	NGB	11.09	13.00	11.89	14.19	**23.24**
Fig. 9(e)	PAN	12.31	12.06	14.40	14.82	**18.31**
	RGB	13.26	17.55	14.34	19.03	**30.28**
	NGB	13.49	17.03	14.86	18.30	**28.71**
Fig. 9(f)	PAN	11.62	11.78	13.50	13.52	**17.82**
	RGB	13.47	13.50	13.98	15.30	**23.34**
	NGB	13.25	14.21	14.50	15.95	**23.97**
Fig. 9(g)	PAN	9.17	6.71	7.73	7.53	**9.97**
	RGB	13.32	14.13	13.98	15.73	**24.90**
	NGB	13.43	14.67	14.55	16.47	**25.68**
Fig. 9(h)	PAN	10.55	10.62	12.77	13.10	**15.30**
	RGB	10.30	9.83	10.79	11.10	**16.52**
	NGB	11.13	12.54	12.31	13.49	**19.98**
Avg.	PAN	11.59	11.17	13.29	13.49	**16.12**
	RGB	11.69	12.20	14.08	14.10	**22.94**
	NGB	11.40	12.98	12.49	14.47	**23.04**

of the proposed method contains more texture details since the singular value of a local gradient of the texture regions is higher than the flat regions [37], [38].

In terms of the processing time for a given test image of size 850×850, Krishnan's and Perrone's methods took about 13.813 s and 3540.400 s, respectively. Pan's methods respectively based on the intensity and dark channel priors took about 142.164 s and 775.227 s. On the other hand, the proposed method took only 1.256, 156.067, and 0.055 s for texture restoration, ℓ_0-norm-based deblurring, and image fusion method, respectively. The computational complexity in the texture restoration in Section II-A is $O(N\log N)$ in the Richardson–Lucy algorithm step, where N is the number of pixels in the image. Activity map estimation and unsharp masking processes require $O(Nm)$ because they use a convolution filter of size m. ℓ_0-norm-based deblurring step in Section II-B requires $O(N^2)$ due to the regularization term consisting of the dark channel and intensity priors. ℓ_2-norm-based fusion method in Section II-C require $O(N\log N)$ because quadratic minimization is solved using FFT.

IV. DISCUSSION

A. Comparison of Different Initial Deblurring Methods

Fig. 14 shows the comparative results of the proposed deblurring method using different initial deblurring methods. In

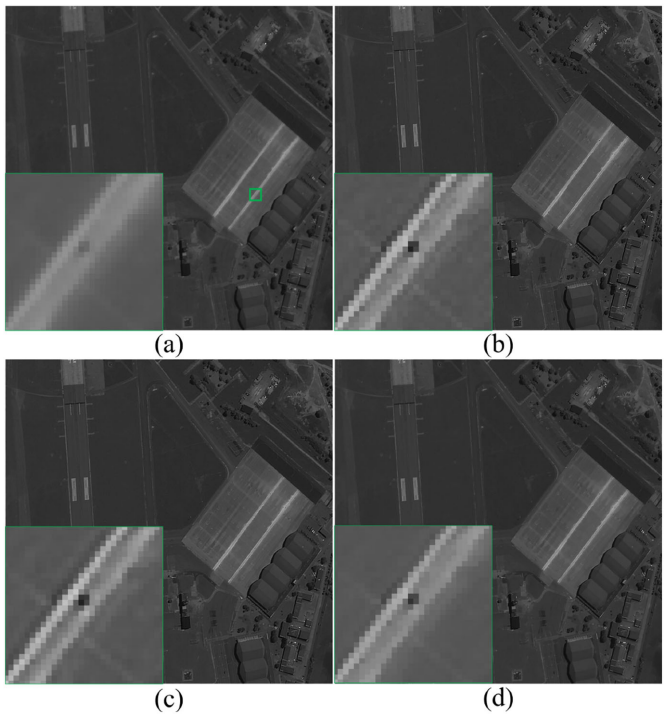

Fig. 14. Comparative results using different initial deblurring methods: (a) an input image, (b) result using the unsharp masking, (c) result using the Richardson–Lucy algorithm, and (d) result using proposed initial deblurring method.

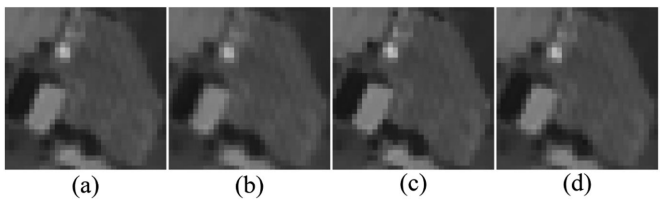

Fig. 15. Comparison of fusion-based deblurring methods on the synthesized blurred image in the PAN band: (a) Krishnan's method [23] (PSNR: 33.6488), (b) Perrone's method [25] (PSNR: 33.88091), (c) Pan's method [29] (PSNR: 32.1519), and (d) Pan's method [30] (PSNR: 33.7803). The results are better viewed in zoomed mode.

Section II-C, the proposed image fusion method minimizes the sum of two ℓ_2-norms: one is the difference between the initially deblurred image and the latent image, and the other is the difference between the ℓ_0-norm-based deblurred result and the latent image. Ringing artifacts in the initially deblurred image can be suppressed by minimizing the second ℓ_2-norm in (16). For that reason, the proposed method adaptively synthesizes the edge region of the result of unsharp masking and texture region of the result of Richardson–Lucy algorithm to reduce the ringing artifact. As a result, the resulting image can avoid the ringing artifact near edges and oversmoothing by ℓ_0-norm-based deblurring preserving the texture region as shown in Fig. 14. In addition, we evaluated the performance of the proposed texture restoration method. Fig. 15 shows the comparative results using the deblurred results of existing methods in the third row of Fig. 10. In this experiment, we fused the deblurred results of

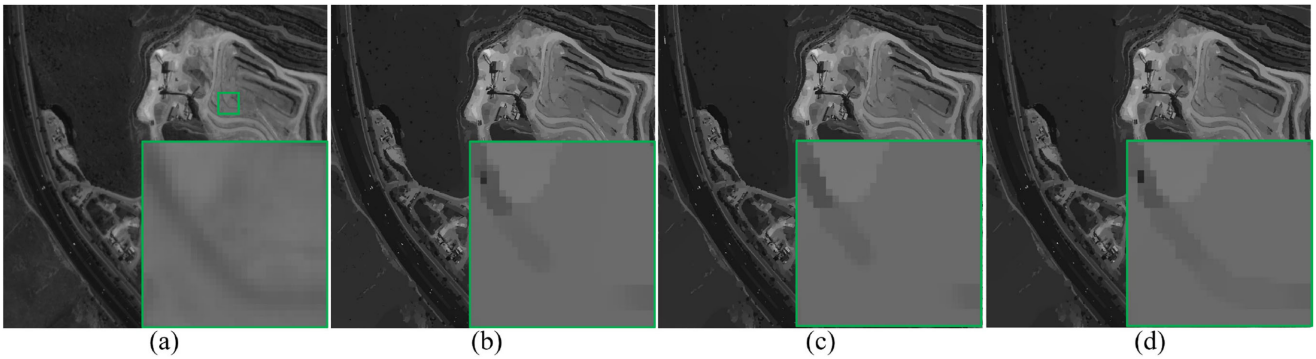

Fig. 16. Comparative results on the ℓ_0-based deblurring image: (a) an input image (Q metric: 11.6722), (b) using only the dark channel prior term (Q metric: 12.7780), (c) using only the intensity prior term (Q metric: 13.8589), and (d) proposed method (Q metric: 12.8755). The regularization parameters μ, γ, and ω were set to 10^{-4}, 10^{-3}, and 10^{-5}, respectively.

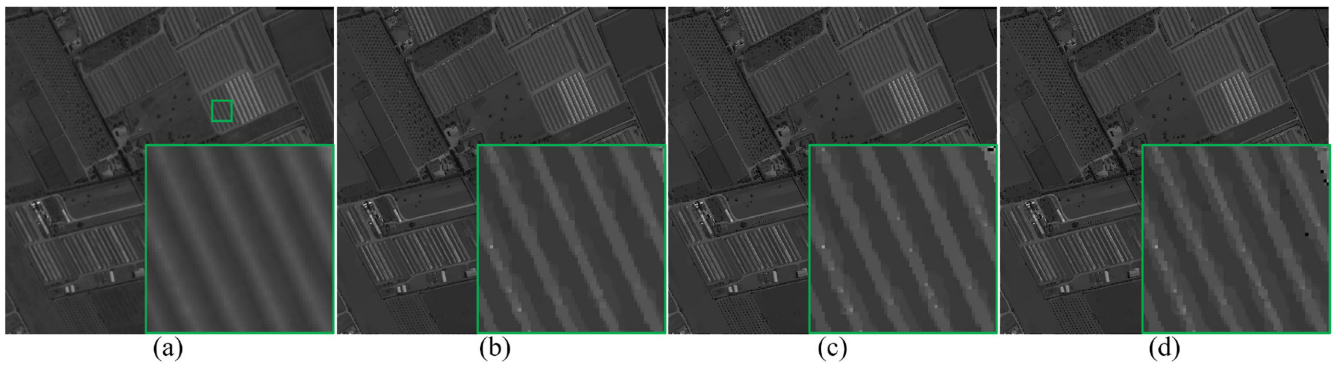

Fig. 17. Comparative results on the ℓ_0-based deblurring image: (a) an input image (Q metric: 12.6730), (b) using only the dark channel prior term (Q metric: 15.1595), (c) using only the intensity prior term (Q metric: 13.4831), and (d) proposed method (Q metric: 13.7258). The regularization parameters μ, γ, and ω were set to 10^{-4}, 10^{-5}, and 10^{-3}, respectively.

existing methods with that of the proposed texture restoration method using (17). As shown in Fig. 15, the proposed method can significantly improve the quality of the deblurred result preserving the texture details in the sense of objective assessment.

B. Comparison of Deblurring Performance Using Different Regularization Terms

In this section, we analyzed the deblurring performance on different regularization terms. In the experiment, we used the test images of size 850×850, which were cropped from PAN band images acquired from KOMPSAT-3A earth observation satellite. To evaluate the performance of the intensity prior, we respectively set $\beta = 0$ for intensity prior, and $\lambda = 8$ for dark channel prior in (6). In terms of dark channel prior, we respectively set $\beta = 8$ for intensity prior and $\lambda = 0$ for dark channel prior. The regularization parameters μ, γ, and ω for the auxiliary variables d, u, and p were set to provide the best deblurring result for each regularization term.

As shown in Figs. 16 and 17, the intensity and dark channel priors cannot preserve the weak texture details and edges with oversmoothing. As described in Section II-B, the intensity prior term helps us to remove the blur of the image because the intensity of the blurred image is higher than that of the clear image for the satellite images as shown in Fig. 4. Since the blurred image is locally constant, the deblurred image using only the intensity prior term cannot preserve the weak edge region with low-intensity value.

In terms of using only the dark channel prior, when the size of the minimum filter is sufficiently large, the dark channel prior can provide better deblurring performance because more dark pixels in large size minimum filter makes the latent image has less bright pixels, which impose more sparsity to the latent image. In conclusion, when the intensity and dark channel priors are combined as the regularization terms, the deblurring can be improved than using individually the intensity and dark channel priors.

Figs. 16(c) and 17(b) provided higher Q metric values, but the resulting images were oversmoothed compared with the proposed method. On the other hand, Figs. 16(d)–17(d) show that the proposed method can provide better-restored result preserving the weak edges in the sense of evaluation.

In addition, we tested deblurring with additive noise to compare the performance in the noisy case. The noisy image in Fig. 18 was obtained by adding white Gaussian noise of

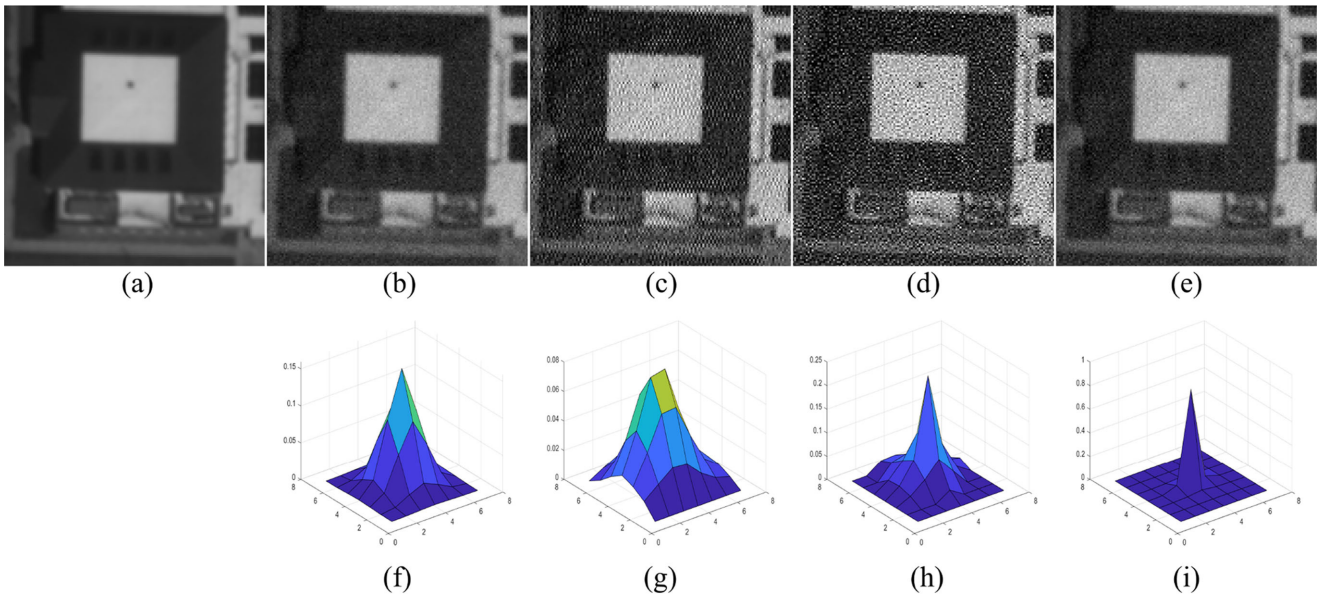

Fig. 18. Comparison of the deblurring performance in the noisy case: (a) blurred image (PSNR: 31.6291 dB), (b) blurred image with additive noise (PSNR: 27.6763 dB), (c) deblurred result using Pan's method (PSNR: 18.6039 dB) [29], (d) deblurred result using another Pan's method (PSNR: 15.9555 dB) [30], (e) deblurred result using the proposed method (PSNR: 25.0927 dB), (f) Gaussian PSF used in the noisy case, (g) estimated PSF using Pan's method (PSNR: 34.8631 dB) [29], (h) estimated PSF using Pan's method (PSNR: 36.3697 dB) [30], and (i) estimated PSF by (18) (PSNR: 20.1395 dB).

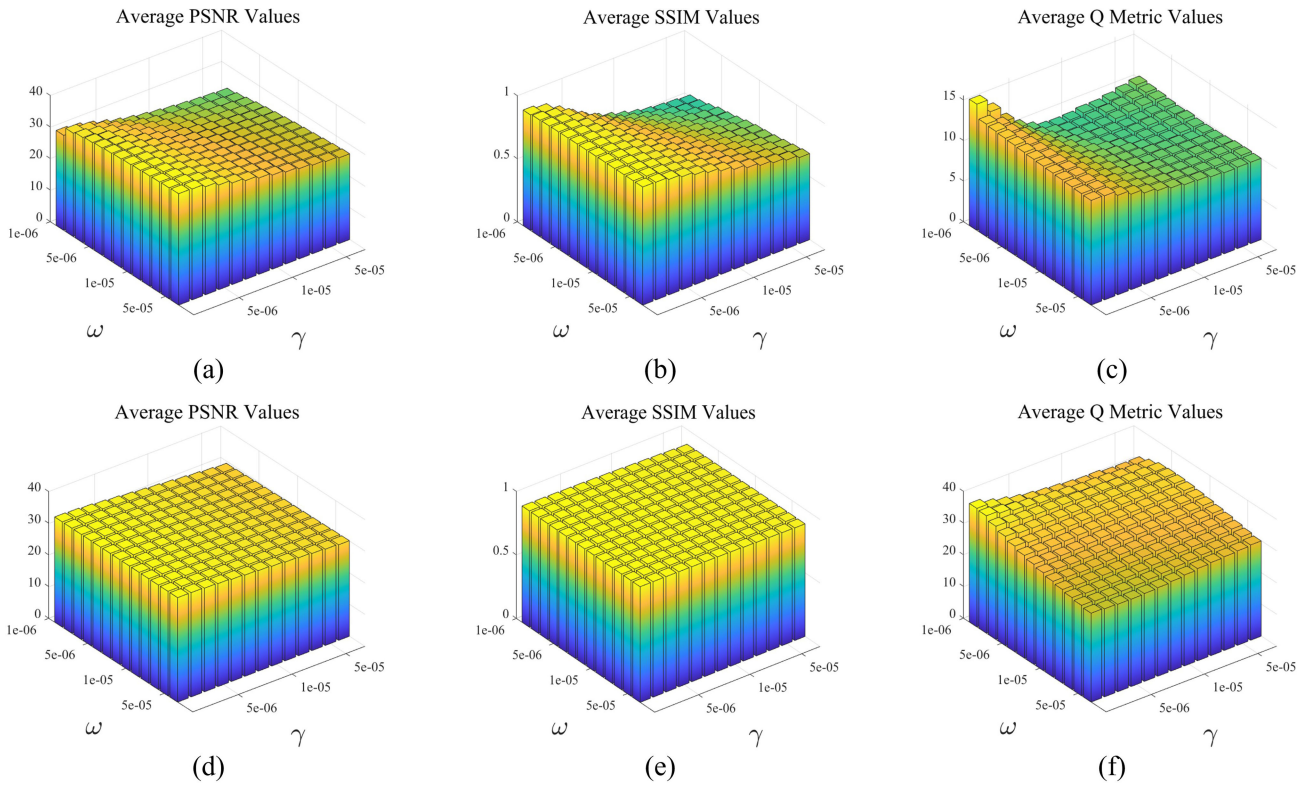

Fig. 19. Sensitivity analysis of the main regularization parameters, ω and γ, used in the proposed method: (a)–(b) PSNR and SSIM values of resulting images using the PAN band shown in Fig. 8, (c) Q metric values of resulting images using the PAN band shown in Fig. 9, (d)–(e) PSNR and SSIM values of resulting images using RGB and NGB bands shown in Fig. 8, and (f) Q metric values of resulting images using RGB and NGB bands shown in Fig. 9.

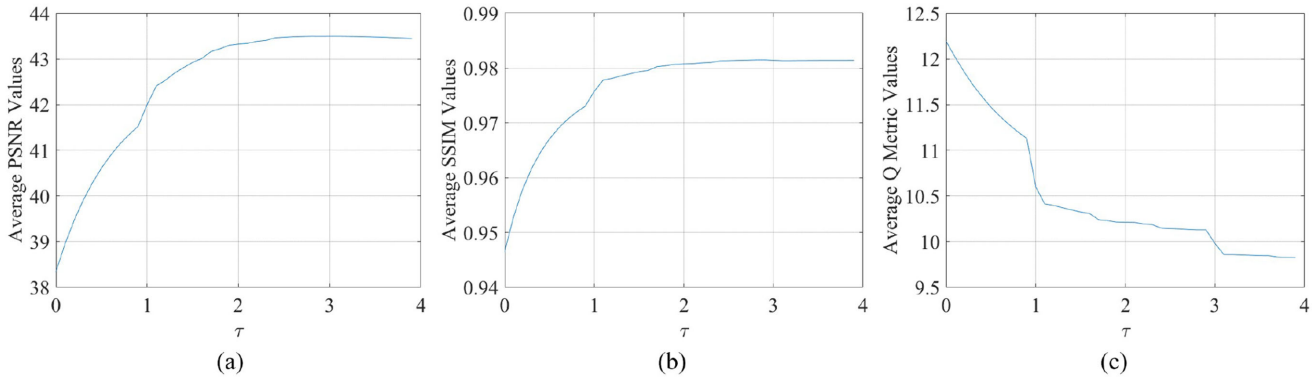

Fig. 20. Sensitivity analysis of the main parameter, denoted as τ. (a) Average PSNR of images shown Fig. 8. (b) Average SSIM of images shown in Fig. 8. (c) Average Q metric values of images shown in Fig. 8.

TABLE III
CONVENTIONS

α	Penalty parameter for the gradient prior
β	Penalty parameter for the intensity prior
∇	$N^2 \times N^2$ block-circulant matrix representing the 2-dimensional derivative operator
$D(\cdot)$	An operator to estimate the dark channel map
d	Auxiliary variables for the gradient prior
η	$N^2 \times 1$ vector representing the additive Gaussian noise images
f	$N^2 \times 1$ vector representing the latent images
γ	Regularization parameter for the dark channel prior
g	$N^2 \times 1$ vector representing the the observed images
g_1	Resulting image of texture restoration
g_2	Resulting image of ℓ_0-norm based deblurring
g_{RL}	Resulting image of Richardson-Lucy deconvolution
g_u	Resulting image of unsharp masking
H	$N^2 \times N^2$ block-circulant matrix generated from a PSF
λ	Penalty parameter for the dark channel prior
μ	Regularization parameter for the gradient prior
$\mathbf{M}$	A linear operator $\mathbf{M}$ applied to the vectorized image f
ω	Regularization parameter for the intensity prior
$\Omega(\mathbf{x})$	Image patch centered at $\mathbf{x}$
Ω_H	The domain of the blur kernel
p	Auxiliary variables for the dark channel prior
ρ	Non-negative regularization parameter for PSF estimation
σ	Tuning parameter to make $w(\cdot)$ distributed as evenly as possible
τ	Non-negative parameter to control the balance between the results g_1 and g_2
u	Auxiliary variables for the intensity prior
$v(\cdot)$	Local variance map
$w(\cdot)$	Activity map

SNR 30 dB. Fig. 18(c)–(e) shows restored results using dark channel [29], intensity prior [30], and the proposed methods, respectively. Both dark channel- and intensity prior-based methods iteratively deblur the input image without considering noise suppression. For this reason, these methods cannot avoid noise amplification and result in lower PSNR values.

On the other hand, the proposed method combines dark channel and intensity prior terms. In (5), ℓ_0-norms $\|\cdot\|_0$ represent the number of nonzero intensities, which cannot effectively reduce the amplification of additive Gaussian noise. The proposed method shows less robust results for noise amplification and has limitations in the noisy case as shown in Fig. 18(e).

C. Parameter Setting

Fig. 19 shows average of PSNR, SSIM, and Q metric values in experimental results to verify the effect of the main parameters γ, ω, and τ in the proposed ℓ_0-norm-based deblurring and image fusion process. For the experiment, WorldView-2/4 and KOMSAT-3A images were used as shown in Figs. 8 and 9. Since Fig. 19(c) and (f) are nonreference images, PSNR and SSIM are not measured. For that reason, KOMSAT-3A images are measured using only Q metric, which is a nonreference measurement criterion. For the ℓ_0-norm-based deblurring process given in (5), we experimentally selected regularization parameters for dark channel prior, intensity prior, and gradient prior, respectively, denoted as γ, μ, and ω. In this article, the proposed method empirically set penalty parameters α, β, and λ to 10^5, 8, and 8, respectively. These parameters control the balance of the gradient, intensity, and dark channel priors. Also, γ and ω were initially set to 10^{-6} and 10^{-3}, respectively, and increased by 8×10^{-5}. Fig. 19(a), (b) shows that PSNR and SSIM were the highest when $\gamma = 9.61 \times 10^{-4}$, and $\omega = 10^{-6}$. Fig. 19(c) also shows that the Q metric value was the highest when $\gamma = 1.61 \times 10^{-4}$, and $\omega = 10^{-6}$. We fixed the gradient prior parameter as $\mu = 10^{-5}$.

As shown in Fig. 19(a)–(c), the larger γ and the smaller ω yield higher average of PSNR, SSIM, Q metric values. Intensity prior is less smoothed because a large ω is less updated in (15), and dark channel prior is expected to have a smoothing effect on the dark channel only when γ is large. On the other hand, Figs. 19(d)–(f) show that RGB and NGB images with lower resolution than PAN band images have the highest PSNR, SSIM, and Q metric values when $\gamma = 10^{-6}$ and $\omega = 10^{-6}$. Since RGB and NGB images have a lower resolution than the pan band images, high γ and ω cause oversmoothing. As a result, high PSNR, SSIM, and Q metric values were obtained when γ and ω were small.

We also performed experiments with various values of τ in (17) for the image fusion process as shown in Fig. 20 τ values were set in the range $[0, 4.0]$ by interval of 0.1. In (17), g_1, g_2 was tested by fixing the result of Sections II-A and II-B and increasing only τ. Since PSNR and SSIM represent similarity of contextual information, the highest value is shown at $\tau = 3.1$. On the other hand, Q metric is the highest at $\tau = 0$ because it represents the degree of structural preservation of the image. However, when $\tau = 0$, the texture detail is lost, so we empirically selected the range of τ values between $[1.5, 3.5]$. The set of variables and parameters are summarized in Table III.

V. Conclusion

In this article, we proposed a novel deblurring method using ℓ_0-norm-based deblurring with the intensity and dark channel priors and ℓ_2-norm-based minimization for adaptive image fusion. In the proposed method, we incorporated the activity map and ℓ_2-norm-based minimization to preserve the texture details of the results of Richardson–Lucy deconvolution and unsharp masking, respectively. In addition, we analyzed that the property of the intensity and dark channel priors of the remote sensing images impose the sparsity to the latent sharp image. Experimental results demonstrated that the proposed method can provide the high-quality restored result preserving both strong edges and texture details without noise amplification and ringing artifact near edges compared with the state-of-the-art methods.

References

[1] M. Wang and R. Li, "Segmentation of high spatial resolution remote sensing imagery based on hard-boundary constraint and two-stage merging," *IEEE Trans. Geosci. Remote Sens.*, vol. 52, no. 9, pp. 5712–5725, Sep. 2014.

[2] X. Zhang, P. Xiao, X. Feng, L. Feng, and N. Ye, "Toward evaluating multiscale segmentations of high spatial resolution remote sensing images," *IEEE Trans. Geosci. Remote Sens.*, vol. 53, no. 7, pp. 3694–3706, Jul. 2015.

[3] S. K. Mylonas, D. G. Stavrakoudis, J. B. Theocharis, and P. A. Mastorocostas, "Classification of remotely sensed images using the genesis fuzzy segmentation algorithm," *IEEE Trans. Geosci. Remote Sens.*, vol. 53, no. 10, pp. 5352–5376, Oct. 2015.

[4] Q. Zhang, Q. Yuan, C. Zeng, X. Li, and Y. Wei, "Missing data reconstruction in remote sensing image with a unified spatial temporal spectral deep convolutional neural network," *IEEE Trans. Geosci. Remote Sens.*, vol. 56, no. 8, pp. 4274–4288, Aug. 2018.

[5] X. Yu, H. Zhang, C. Luo, H. Qi, and P. Ren, "Oil spill segmentation via adversarial f-divergence learning," *IEEE Trans. Geosci. Remote Sens.*, vol. 56, no. 9, pp. 4973–4988, Sep. 2018.

[6] W. Ao, F. Xu, Y. Li, and H. Wang, "Detection and discrimination of ship targets in complex background from spaceborne ALOS-2 SAR images," *IEEE J. Sel. Topics Appl. Earth Observ. Remote Sens.*, vol. 11, no. 2, pp. 536–550, Feb. 2018.

[7] C. Niu, J. Zhang, Q. Wang, and J. Liang, "Weakly supervised semantic segmentation for joint key local structure localization and classification of aurora image," *IEEE Trans. Geosci. Remote Sens.*, vol. 56, no. 12, pp. 7133–7146, Dec. 2018.

[8] Z. Deng, H. Sun, S. Zhou, J. Zhao, and H. Zou, "Toward fast and accurate vehicle detection in aerial images using coupled region-based convolutional neural networks," *IEEE J. Sel. Topics Appl. Earth Observ. Remote Sens.*, vol. 10, no. 8, pp. 3652–3664, Aug. 2017.

[9] G. Chen, X. Zhang, Q. Wang, F. Dai, Y. Gong, and K. Zhu, "Symmetrical dense-shortcut deep fully convolutional networks for semantic segmentation of very-high-resolution remote sensing images," *IEEE J. Sel. Topics Appl. Earth Observ. Remote Sens.*, vol. 11, no. 5, pp. 1633–1644, May 2018.

[10] R. Li, W. Liu, L. Yang, S. Sun, W. Hu, F. Zhang, and W. Li, "Deepunet: A deep fully convolutional network for pixel-level sea-land segmentation," *IEEE J. Sel. Topics Appl. Earth Observ. Remote Sens.*, vol. 11, no. 11, pp. 3954–3962, Nov. 2018.

[11] R. Shirvany, M. Chabert, and J. Tourneret, "Ship and oil-spill detection using the degree of polarization in linear and hybrid/compact dual-pol sar," *IEEE J. Sel. Topics Appl. Earth Observ. Remote Sens.*, vol. 5, no. 3, pp. 885–892, Jun. 2012.

[12] X. Zhu and P. Milanfar, "Stabilizing and deblurring atmospheric turbulence," in *Proc. IEEE Int. Conf. Comput. Photography*, 2011, pp. 1–8.

[13] X. Zhao, F. Wang, T. Huang, M. K. Ng, and R. J. Plemmons, "Deblurring and sparse unmixing for hyperspectral images," *IEEE Trans. Geosci. Remote Sens.*, vol. 51, no. 7, pp. 4045–4058, Jul. 2013.

[14] K. Gao, Z. Zhu, Z. Dou, and L. Han, "Variable exponent regularization approach for blur kernel estimation of remote sensing image blind restoration," *IEEE Access*, vol. 6, pp. 4352–4374, 2018.

[15] H. Shen, W. Zhao, Q. Yuan, and L. Zhang, "Blind restoration of remote sensing images by a combination of automatic knife-edge detection and alternating minimization," *Remote Sens.*, vol. 6, no. 8, pp. 7491–7521, 2014.

[16] M. Azadbakht, C. Fraser, and K. Khoshelham, "A sparsity-based regularization approach for deconvolution of full-waveform airborne lidar data," *Remote Sens.*, vol. 8, no. 8, 2016, Art. no. 648.

[17] Z.-J. Liu, C.-Y. Wang, and C.-F. Luo, "Estimation of CBERS-1 point spread function and image restoration," *J. Remote Sens.*, vol. 8, no. 3, pp. 238–244, 2004.

[18] D. Fish, A. Brinicombe, E. Pike, and J. Walker, "Blind deconvolution by means of the Richardson–Lucy algorithm," *J. Opt. Soc. Amer. A*, vol. 12, no. 1, pp. 58–65, 1995.

[19] Q. Shan, W. Xiong, and J. Jia, "Rotational motion deblurring of a rigid object from a single image," in *Proc. IEEE 11th Int. Conf. Comput. Vision*, 2007, pp. 1–8.

[20] R. Fergus, B. Singh, A. Hertzmann, S. T. Roweis, and W. T. Freeman, "Removing camera shake from a single photograph," *ACM Trans. Graph.*, vol. 25, no. 3, pp. 787–794, 2006.
[21] L. Yuan, J. Sun, L. Quan, and H.-Y. Shum, "Image deblurring with blurred/noisy image pairs," *ACM Trans. Graph.*, vol. 26, no. 3, 2007, Art. no. 1.
[22] L. Xu, C. Lu, Y. Xu, and J. Jia, "Image smoothing via l0 gradient minimization," *ACM Trans. Graph.*, vol. 30, no. 6, 2011, Art. no. 174.
[23] D. Krishnan, T. Tay, and R. Fergus, "Blind deconvolution using a normalized sparsity measure," in *Proc. IEEE Conf. Comput. Vision Pattern Recognit.*, 2011, pp. 233–240.
[24] H. Shen, L. Du, L. Zhang, and W. Gong, "A blind restoration method for remote sensing images," *IEEE Geosci. Remote Sens. Lett.*, vol. 9, no. 6, pp. 1137–1141, Nov. 2012.
[25] D. Perrone and P. Favaro, "A clearer picture of total variation blind deconvolution," *IEEE Trans. Pattern Anal. Mach. Intell.*, vol. 38, no. 6, pp. 1041–1055, Jun. 2016.
[26] R. C. Gonzalez and R. E. Woods, *Digital Image Processing*, 3rd ed., Upper Saddle River, NJ, USA: Prentice-Hall, 2006.
[27] S. N. Efstratiadis and A. K. Katsaggelos, "Adaptive iterative image restoration with reduced computational load," *Opt. Eng.*, vol. 29, no. 12, pp. 1458–1468–11, Dec. 1990.
[28] K. He, J. Sun, and X. Tang, "Single image haze removal using dark channel prior," *IEEE Trans. Pattern Anal. Mach. Intell.*, vol. 33, no. 12, pp. 2341–2353, Dec. 2011.
[29] J. Pan, D. Sun, H. Pfister, and M. Yang, "Blind image deblurring using dark channel prior," in *Proc. IEEE Conf. Comput. Vision Pattern Recognit.*, Jun. 2016, pp. 1628–1636.
[30] J. Pan, Z. Hu, Z. Su, and M. Yang, "l_0-regularized intensity and gradient prior for deblurring text images and beyond," *IEEE Trans. Pattern Anal. Mach. Intell.*, vol. 39, no. 2, pp. 342–355, Feb. 2017.
[31] D. Zoran and Y. Weiss, "From learning models of natural image patches to whole image restoration," in *Proc. Int. Conf. Comput. Vision*, 2011, pp. 479–486.
[32] Y. Yan, W. Ren, Y. Guo, R. Wang, and X. Cao, "Image deblurring via extreme channels prior," in *Proc. IEEE Conf. Comput. Vision Pattern Recognit.*, Jul. 2017, pp. 6978–6986.
[33] J. Shin, M. Kim, J. Paik, and S. Lee, "Radiance reflectance combined optimization and structure-guided ℓ_0-norm for single image dehazing," *IEEE Trans. Multimedia*, vol. 22, no. 1, pp. 30–44, Jan. 2020.
[34] K. Koh, S.-J. Kim, and S. Boyd, "An interior-point method for large-scale l1-regularized logistic regression," *J. Mach. Learn. Res.*, vol. 8, pp. 1519–1555, Dec. 2007.
[35] Z. Wang, A. C. Bovik, H. R. Sheikh, and E. P. Simoncelli, "Image quality assessment: From error visibility to structural similarity," *IEEE Trans. Image Process.*, vol. 13, no. 4, pp. 600–612, Apr. 2004.
[36] Harris Geospatial Solutions, Inc., "Worldview-4," [Online]. Available: https://www.harrisgeospatial.com/Data-Imagery/Satellite-Imagery/High-Re% solution/WorldView-4, 2019. Accessed: Jun. 11, 2019.
[37] X. Zhu and P. Milanfar, "Automatic parameter selection for denoising algorithms using a no-reference measure of image content," *IEEE Trans. Image Process.*, vol. 19, no. 12, pp. 3116–3132, Dec. 2010.
[38] J. Yang, Z. Lin, and S. Cohen, "Fast image super-resolution based on in-place example regression," in *Proc. IEEE Conf. Comput. Vision Pattern Recognit.*, Jun. 2013, pp. 1059–1066.

Heunseung Lim (Student Member, IEEE) was born in Yeosu, South Korea, in 1995. He received the B.S. degree in information and communication engineering from Sunmoon University, Asan, South Korea, in 2018. He received the M.S degree in image engineering from Chung-Ang University, Seoul, South Korea, in 2020, where he is currently working toward the Ph.D. degree in image engineering.

His research interests include deblur, remote sensing images, image enhancement, and restoration.

Soohwan Yu (Student Member, IEEE) was born in Incheon, South Korea, in 1988. He received the B.S. degree in information and communication engineering from Suwon University, Gyeonggi, South Korea, in 2013. He received the M.S degree in image engineering from Chung-Ang University, Seoul, South Korea, in 2016, where he is currently working toward the Ph.D. degree in image engineering.

His research interests include image enhancement, super-resolution, and image restoration.

Kwanwoo Park was born in Ulsan, South Korea, in 1994. He received the B.S. and M.S. degrees in integrative engineering and image engineering from Chung-Ang University, Seoul, South Korea, in 2017 and 2019, respectively.

He is currently researching the computer vision algorithms with Autonomous Driving Laboratory, PLK Technology, South Korea. His research interests include object detection, machine learning, and deep learning.

Doochun Seo received the Ph.D. degree in civil engineering from Gyeongsang National University, Jinju, South Korea, in 2002.

He has been with Korea Aerospace Research Institute since 2002, and has been a Principle Researcher of Satellite Operation & Application Center since 2015. He has been a Chief Engineer of the Calibration and Validation for the KOMPSAT series with Korea Aerospace Research Institute, DaeJeon, since 2005. He primary research interests and back ground are in satellite photogrammetry, sensor modeling, DEM, ortho-image generation and geometric calibration of high resolution satellite image data.

Joonki Paik (Senior Member, IEEE) was born in Seoul, South Korea, in 1960. He received the B.S. degree in control and instrumentation engineering from Seoul National University, Seoul, South Korea, in 1984, and the M.S. and Ph.D. degrees in electrical engineering and computer science from Northwestern University, Evanston, IL, USA, in 1987 and 1990, respectively.

From 1990 to 1993, he was a Senior Research Engineer with Samsung Electronics, where he designed image stabilization chip sets for consumer camcorders. Since 1993, he has been a member of the faculty at Chung-Ang University, Seoul, South Korea, where he is currently the Dean of the Graduate School of Advanced Imaging Science, Multimedia, and Film. From 1999 to 2002, he was a Visiting Research Professor with the Department of Electrical and Computer Engineering, University of Tennessee, Knoxville. He has served the Consumer Electronics Society of the IEEE as a member of the Editorial Board. Since 2005, he has been the Head of the National Research Laboratory in the field of image processing and intelligent systems. From 2005 to 2007, he served as the Dean of the Graduate School of Advanced Imaging Science, Multimedia, and Film. From 2005 to 2007, he was the Director of the Seoul Future Contents Convergence Cluster (SFCC). In 2008, he was a full-time technical consultant for the System LSI Division of Samsung Electronics, where he developed various computational photographic techniques, including an extended depth of field system. He has served as a member of the Presidential Advisory Board for Scientific/Technical Policy with the Korean Government and a Technical Consultant for the Korean Supreme Prosecutor's Office for computational forensics.

Dr. Paik was a two-times recipient of the Chester-Sall Award from the IEEE Consumer Electronics Society, Academic Award from the Institute of Electronic Engineers of Korea, and a Best Research Professor Award from Chung-Ang University.